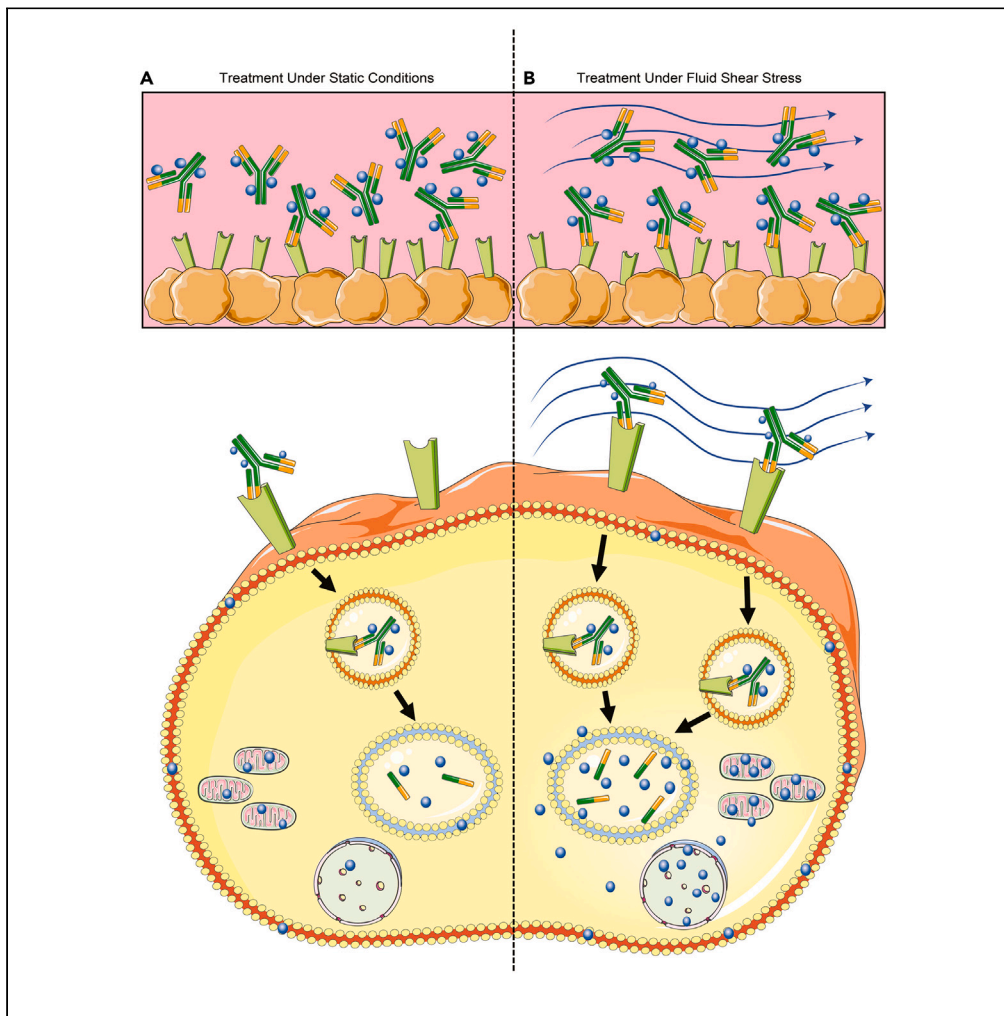**Article**

Transient fluid flow improves photoimmunoconjugate delivery and photoimmunotherapy efficacy

Aaron J. Sorrin,
Keri Zhou,
Katherine May, ...,
Imran Rizvi, Dana
M. Roque, Huang-
Chiao Huang

hchuang@umd.edu

Highlights

Fluid flow enhances
targeted delivery of
photoimmunoconjugates
to cancer cells

Fluid flow can alter the
subcellular localization of
photoimmunoconjugates

Fluid flow-enhanced
delivery of photosensitizer
leads to superior PDT
outcomes

Article

Transient fluid flow improves photoimmunoconjugate delivery and photoimmunotherapy efficacy

Aaron J. Sorrin,[1] Keri Zhou,[1] Katherine May,[1] Cindy Liu,[1] Kathryn McNaughton,[1] Idrisa Rahman,[1] Barry J. Liang,[1] Imran Rizvi,[2,3] Dana M. Roque,[4,5] and Huang-Chiao Huang[1,5,6,*]

SUMMARY

Circulating drugs in the peritoneal cavity is an effective strategy for advanced ovarian cancer treatment. Photoimmunotherapy, an emerging modality with potential for the treatment of ovarian cancer, involves near-infrared light activation of antibody-photosensitizer conjugates (photoimmunoconjugates) to generate cytotoxic reactive oxygen species. Here, a microfluidic cell culture model is used to study how fluid flow-induced shear stress affects photoimmunoconjugate delivery to ovarian cancer cells. Photoimmunoconjugates are composed of the antibody, cetuximab, conjugated to the photosensitizer, and benzoporphyrin derivative. Longitudinal tracking of photoimmunoconjugate treatment under flow conditions reveals enhancements in subcellular photosensitizer accumulation. Compared to static conditions, fluid flow-induced shear stress at 0.5 and 1 dyn/cm^2 doubled the cellular delivery of photoimmunoconjugates. Fluid flow-mediated treatment with three different photosensitizer formulations (benzoporphyrin derivative, photoimmunoconjugates, and photoimmunoconjugate-coated liposomes) led to enhanced phototoxicity compared to static conditions. This study confirms the fundamental role of fluid flow-induced shear stress in the anti-cancer effects of photoimmunotherapy.

INTRODUCTION

Cancer cells in the abdominal cavity are continuously exposed to fluid shear stress (FSS) from accumulated malignant fluids (ascites). Patients with advanced stage or recurrent ovarian cancer can present with over two liters of ascites in the peritoneal cavity.[1] The shear stresses conferred by currents of ascitic fluid resulting from organ mobility, gravity, breathing, and other bodily movements are estimated to be 5 dyn/cm^2 or less.[2–5] To date, most research has been dedicated to exploring the impact of ascitic FSS on cell proliferation, migration, vitality, metabolism, expression of genes and proteins, and other cellular functions. Overall, these studies have found that "continuous" (days or weeks) FSS may induce epithelial-mesenchymal transition, increased motility, morphological changes, or treatment resistance.[6–9] On the other hand, "transient" (minutes to hours) fluid flow is already used medically to distribute the chemotherapy solution in the abdomen of patients with peritoneal carcinomatosis for improved outcomes.[10] With new molecular-targeted theranostic agents and nanomedicines under development for peritoneally disseminated tumors, there is a need to enhance our basic understanding of transient FSS as a potential tool in the arsenal against cancer.

An emerging theranostic treatment for peritoneally disseminated ovarian cancer is photoimmunotherapy (PIT). PIT is a molecular-targeted modality that leverages targeting properties of antibodies for selective delivery of photosensitizers via their conjugation as photoimmunoconjugates (PICs).[11,12] Upon light absorption by photosensitizers, highly cytotoxic reactive oxygen species are generated for the ablation of cancer cells and priming of the surviving cells for adjuvant treatments.[11] In addition to the cytotoxic effects of PIT, the fluorescent signal generated from the photosensitizers on the PIC can be used for cancer imaging.[12] PIT was first described by Mew et al. who conjugated myosarcoma-targeted monoclonal antibodies to hematoporphyrin.[13] Since then, several antibody-photosensitizer combinations have been developed for the photochemical treatment and diagnosis of cancer.[11]

[1]Fischell Department of Bioengineering, University of Maryland, College Park, MD 20742, USA

[2]Joint Department of Biomedical Engineering, University of North Carolina at Chapel Hill, Chapel Hill, NC, North Carolina State University, Raleigh, NC 27599, USA

[3]Lineberger Comprehensive Cancer Center, School of Medicine, University of North Carolina at Chapel Hill, Chapel Hill, NC 27599, USA

[4]Department of Obstetrics, Gynecology and Reproductive Sciences, University of Maryland School of Medicine, Baltimore, MD 21201, USA

[5]Marlene and Stewart Greenebaum Cancer Center, University of Maryland School of Medicine, Baltimore, MD 21201, USA

[6]Lead contact

*Correspondence:
hchuang@umd.edu

https://doi.org/10.1016/j.isci.2023.107221

Much of the preclinical and clinical research on PIT targets the epidermal growth factor receptor (EGFR).[14–16] EGFR-targeted PIT was shown to selectively induce killing of EGFR-expressing ovarian cancer cells while mitigating EGFR signaling pathways.[17] Importantly, these findings highlight that antibodies used in PIT retain biological functions to achieve multi-pronged anti-cancer effects of both photosensitizer delivery and inhibition of tumor-promoting cell signaling. Consistent with these dual functions, we and others have shown that PICs targeting the EGFR can attenuate EGFR and extracellular signal-regulated kinases 1/2 (ERK1/2) signaling.[17,18] Nonetheless, one of the major challenges associated with PIT is limited photosensitizer delivery to cancer cells.[18–20] This can be attributed to several factors including finite antigen numbers per cancer cell, limited number of photosensitizer-to-antibody payload, and poor tumor accessibility of antibodies.[20] This study overcomes this limitation through the rigorous examination of transient flow as a drug delivery platform to enhance total cellular PIC delivery and thereby bolster cytotoxic effects.

In addition to total cellular PIC delivery, the subcellular localization is another key determinant of PIT treatment effect.[21–24] Upon antibody-EGFR binding in the plasma membrane, the complex rapidly undergoes receptor-mediated endocytosis followed by localization in the endosome, lysosome, endoplasmic reticulum, and nucleus.[25–28] Prior work shows that lysosomal digestion of EGFR-targeted PIC dequenches the photosensitizer, enabling applications for PIT and imaging.[12,29] Despite extensive investigations of subcellular PIC accumulation under static conditions, the role of transient flow as a modulator of these processes remains largely unknown. Results from this study confirm time- and FSS-dependent effects of transient flow on PIC subcellular accumulation.

PIT is achieved in this study using US Food and Drug Administration agents: cetuximab, an EGFR-targeted antibody, and benzoporphyrin derivative (BPD), a photosensitizer. A perfusion system is used to treat OVCAR8 ovarian cancer cells at varying FSS (0.5–5 dyn/cm^2, 1.16–11.55 mL/min; Table S1). Microfluidic models strike an optimal balance between the simplicity/reductionism of *in vitro* models with the complexity/realism of animal models, making them ideal to study the effects of FSS.[2,30] Longitudinal binding studies reveal time-dependent changes in subcellular uptake that vary between static and FSS conditions. The results also reveal significant effects of FSS in promoting total cellular photosensitizer uptake while modulating subcellular compartmentalization. Toxicity studies are performed with multiple photosensitizer formulations including free BPD, PIC, and our published liposomal PIC formulation (PIC-Nal).[19] Across all formulations, FSS-mediated delivery induces heightened cell killing. Results from this work implicate transient flow as a fundamental property for consideration in the implementation of photochemical treatments for locally disseminated metastases.

RESULTS

PIC stability and cell viability are maintained under transient FSS, while EGFR expression is modestly attenuated

A model for the delivery of photodynamic agents under FSS culture was established using the ibidi Pump System and μ-Slide I$^{0.6}$ Luer chips (ibidi). This model was first implemented for the evaluation of flow-induced changes in PIC purity and cellular properties (Figures 1A–1C). Purity was evaluated to ensure that treatment under FSS conditions would not compromise PIC conjugation. In these experiments, PIC was run through the pump for 30 min at 1 dyn/cm^2 in cell culture medium or PBS. Perfusate was then collected and subjected to gel electrophoresis for imaging of fluorescence (ex/em: 435/700) and total protein (Figures 1A and 1B). The quantified purity data (Figure 1C) revealed that PICs retained purity following FSS culture conditions. Next, drug-free experiments were performed to evaluate the cellular effects of transient FSS (30 min, 1 dyn/cm^2). Figure 1D shows that flow conditions did not cause significant alterations in cell viability (analyzed by neutral red uptake (NRU) assay) compared to static controls. Images of cells following culture in static and flow conditions showed no significant morphological differences (Figure 1E). Quantification of cellular EGFR expression revealed a 13% decrease (p < 0.05) following FSS culture (30 min, 1 dyn/cm^2) (Figures 1F and 1G).

Longitudinal binding analysis reveals that transient FSS modulates PIC-based BPD localization in a time-dependent manner

Next, the role of FSS in longitudinally modulating subcellular photosensitizer compartmentalization was examined. Data in the plasma membrane and organelle compartments revealed a time-dependent increase in BPD accumulation over time, reaching an observable plateau by 3 h at ~0.24 pmol and ~0.28 pmol, respectively (Figures 2A and 2B). No significant differences in plasma membrane protein levels
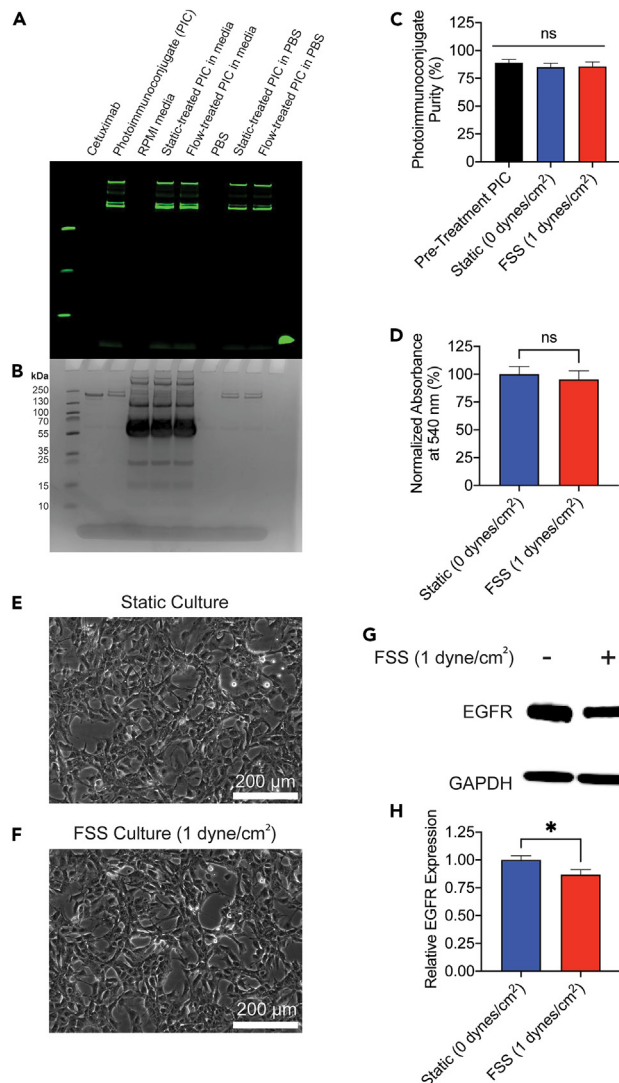
Figure 1. Transient fluid shear stress-induced effects on PIC purity, cell viability, and EGFR expression

(A–C) Comparison of PIC purity following incubation under static or flow conditions. Cell viability (D), morphology (E and F), and EGFR expression (G and H) were evaluated following drug-free treatment under static or 1 dyn/cm^2 conditions for 30 min. Statistical analysis was performed using one-way ANOVA (C) and t tests (D and H). Error bars represent the standard error of the mean. *$p \leq 0.05$; ns: nonsignificant.

were observed, though a significant increase from 4.08 to 11.34 μg protein ($p < 0.01$) was observed for the organelle compartment at 30 min. Longitudinal data for the nuclear compartment reveal overall more BPD following FSS culture, with statistically significant increases at 30 min and 300 min ($p < 0.01$) (Figure 2C). Nuclear protein remained unchanged longitudinally between static and flow conditions. In the cytosolic compartment, which contains the most cellular proteins, higher amounts of BPD are observed under FSS treatment conditions compared to static, with a significant increase at 240 min ($p < 0.05$) (Figure 2D). Total BPD was normalized to protein (Figure S2) to analyze changes in BPD with consideration for protein modulation within each compartment. Fold changes in BPD/protein averaged across all time points from 10 to 300 min revealed that FSS-mediated PIC delivery changes uptake by 1.01-fold, 0.97-fold, 2.52-fold, and 7.03-fold in the plasma membrane, organelle, nuclear, and cytosol fractions, respectively.

Total cellular uptake varies with FSS

Following PIC treatment under 0, 0.5, 1, or 5 dyn/cm^2, total cellular BPD and protein were quantified (Figure 3). While FSS-mediated PIC treatment did not induce significant changes in total cellular protein,
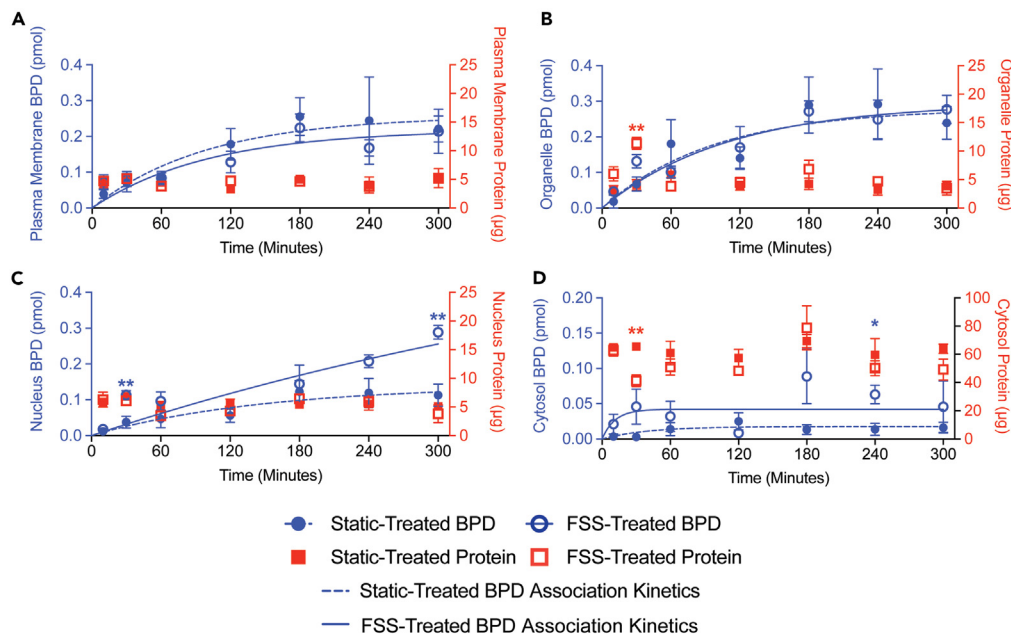
Figure 2. Longitudinal monitoring of subcellular photosensitizer and protein under transient fluid shear stress

Confluent monolayers of OVCAR8 cells were treated with 1 µM PIC under static or FSS (5 dyn/cm^2) conditions for 10, 30, 60, 120, 180, 240, and 300 min. At each time point, cells were fractionated using Minute Plasma Membrane Protein Isolation and Cell Fractionation Kit (Invent Biotechnologies, Inc.). Longitudinal data for total BPD and protein are plotted for the plasma membrane (A), organelle compartment (B), nucleus (C), and cytosol (D). BPD association profiles are shown for the groups treated under static and FSS conditions with a dotted blue line and a solid blue line, respectively. Statistical analysis was performed using t tests at each time point. Error bars represent the standard error of the mean. *p ≤ 0.05; **p ≤ 0.01; ns: nonsignificant.

cellular BPD increased from 0.42 to 0.79 pmol (p < 0.05), 0.74 pmol (p < 0.01), and 0.63 pmol for 0.5, 1, and 5 dyn/cm^2, respectively (Figure 3A). Results for total BPD vs. total cellular protein are plotted in Figure 3B. Groups treated under FSS tend to cluster higher on the graph with respect to the y axis (BPD). Normalized BPD/protein increased under FSS conditions by 1.95-fold (p < 0.01), 1.71-fold (p < 0.01), and 1.62-fold for 0.5, 1, and 5 dyn/cm^2, respectively (Figure 3C). Considering the heterogeneity of ovarian cancers, we next investigated PIC uptake under static versus FSS conditions (1 dyn/cm^2) of a secondary high-grade serous cell line, OVCAR3 (Figure S3). PIC delivery to OVCAR3 cells, measured in BPD normalized to protein, increased under FSS by ~70%.

Varying FSS modulates subcellular photosensitizer localization and compartmentalization

FSS-dependent variations in subcellular localization (Figure 4) and compartmentalization (Figure 5) were characterized. For all subcellular compartments, FSS culture during photosensitizer treatment enhanced BPD accumulation at all flow rates compared to the static control (Figures 4A–4D). BPD localization in the plasma membrane increased from 0.057 pmol at 0 dyn/cm^2 to 0.079, 0.135, and 0.081 pmol for 0.5, 1, and 5 dyn/cm^2, respectively. In the organelle compartment, BPD in static groups averaged 0.087 pmol, whereas increases in moles of BPD to 0.125, 0.187 (p < 0.01), and 0.131 pmol were observed at 0.5, 1, and 5 dyn/cm^2, respectively. Nuclear BPD localization increased drastically under FSS-mediated treatment, with 0.037 pmol under static conditions increasing to 0.147 (p < 0.01), 0.191 (p < 0.0001), and 0.113 (p < 0.05) pmoles at 0.5, 1, and 5 dyn/cm^2, respectively. Cytosolic BPD was approximately 0 pmol following PIC incubation under static culture for 30 min but increased to 0.049, 0.152 (p < 0.001), and 0.046 pmol with increasing FSS. Variations in compartmental protein levels were less consistent, though some significant changes were revealed. In the plasma membrane, protein increased significantly between 0 and 1 dyn/cm^2 (5.22–10.57 µg, p < 0.05). In the organelle compartment, protein increased from 4.78 to 11.34 µg (p < 0.05) at 0 and 5 dyn/cm^2, respectively. No significant changes in nuclear protein were observed, though cytosolic protein decreased from 65.51 µg at 0 dyn/cm^2 to 41.20 µg at 5 dyn/cm^2 (p < 0.05).
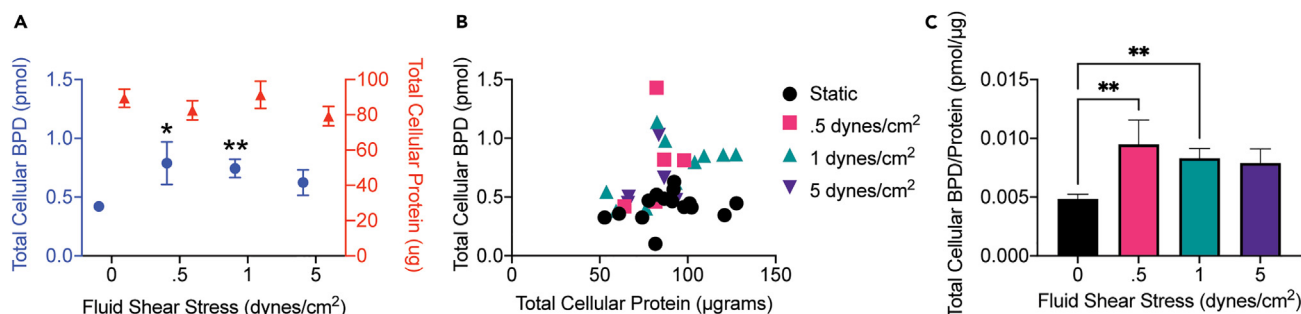
Figure 3. Comparison of total BPD, total protein, and BPD/protein at varying fluid shear stresses

OVCAR8 cell monolayers plated µ-Slide $I^{0.6}$ Luer chips were treated with 1 µM PIC for 30 min under static or FSS (0.5, 1, 5 dyn/cm^2) conditions. Total BPD and protein were quantified by UV-Vis spectrophotometry and BCA, respectively. Averaged data (A) and individual datapoints (B) are shown, as well as the normalized BPD/protein (C). Statistical analysis was performed using a one-way ANOVA, and FSS data were compared to static controls using post hoc Dunnet test. Error bars represent the standard error of the mean. *$p \leq 0.05$; **$p \leq 0.01$; ns: nonsignificant.

Trends in BPD vs. protein were next explored (Figures 4E–4H). Plasma membrane data revealed that FSS conditions enhanced BPD and protein levels compared to static conditions. In the organelle compartment, nearly all the FSS-cultured groups showed higher amounts of total protein, and most showed higher amounts of BPD uptake, with respect to the static controls. Within the nuclear fraction, FSS data are loosely grouped above static with respect to the y axis, without consistent differences along the x axis (protein). In the cytosol, there are no clear trends in grouping of protein levels with varied FSS, though BPD is observably higher for most groups treated under FSS. Next, BPD was normalized to protein (Figures 4I–4L), revealing notable increases in the nuclear compartment from 0.005 at 0 dyn/cm^2 to 0.019, 0.024 ($p < 0.01$), and 0.019 ($p < 0.05$) pmoles/µgram at 0.5, 1, and 5 dyn/cm^2, respectively. In the cytosol compartment, BPD/protein increased from ~4e-5 pmol/µgram at the static condition by 50-fold at 1 dyn/cm^2 ($p < 0.01$) and ~20-fold at 0.5 and 5 dyn/cm^2. Percentage of total cellular BPD and protein contained within each subcellular compartment was next investigated (Figure 5). BPD and protein values were summed across all fractions; then values in each fraction were divided by the sum to determine percentages. Under flow, percent BPD decreased in the organelle fraction and increased in nuclear and cytosol fractions (Figure 5A). Organelle-localized percent protein increases from 6% under static treatment to ~13% under flow (Figure 5B). Cytosolic percent protein reveals a concomitant decrease from 80% under static treatment to an average of 68% under flow. Confocal microscopy was used to further confirm enhanced PIC delivery under FSS conditions (Figure S4).

Transient flow-mediated delivery enhances cytotoxicity of three photosensitizer formulations in a light dose-dependent manner

Next, cytotoxicity of photodynamic agents delivered under static or FSS conditions was assessed. Multiple formulations were included to evaluate variations across free photosensitizer (BPD), antibody-conjugated photosensitizer (PIC), and liposome-conjugated PIC (PIC-Nal) (Figure S5). The PIC-Nal formulation was previously developed by us.[19] PIC-Nal size, PDI, zeta potential, and stability under FSS were tested (Table S2; Figure S6). There were no significant differences in size and PDI between FSS-treated and static-treated PIC-Nal after 30 min or 2 h, indicating overall stability. Photoactivity was quantified for all formulations (Figure S7), revealing 0.6%, 3.4%, and 10.6% photoactivity for BPD, PIC, and PIC-Nal, respectively. For PIC-treated groups, cell viability decreased with flow treatment from 89% to 74%, 80% to 65.5% ($p < 0.05$), 76% to 64.25% ($p < 0.001$), and 62.7% to 51% ($p < 0.05$) for 10, 20, 40, and 80 J/cm^2, respectively (Figure 6A). For cells treated with PIC-Nal, flow treatment decreased viability from 88% to 86.3%, 81% to 67.7%, 73% to 65%, and 67.7% to 50% ($p < 0.01$) at 10, 20, 40, and 80 J/cm^2, respectively (Figure 6B). Free BPD induced the most potent cytotoxicity, which was improved further still by flow-mediated delivery from 60% to 45%, 47.7% to 27.3% ($p < 0.05$), 35% to 15.3% ($p < 0.01$), and 12.7% to 5% at each increasing light dose (Figure 6C). Next, total cellular photosensitizer uptake profiles were compared between each photosensitizer formulation (Figures 6D–6F). Consistent with the cytotoxicity data, FSS-mediated delivery enhanced total cellular uptake across all formulations. Uptake improved under flow by ~67% for BPD ($p < 0.001$), 60% for PIC ($p < 0.001$), and ~43% for PIC-Nal. We also confirmed, using EGFR-negative cells (J774), that the FSS-enhanced uptake of PIC is dependent on EGFR expression. While BPD uptake by J774 cells increased significantly under FSS, PIC uptake did not change (Figure S8).
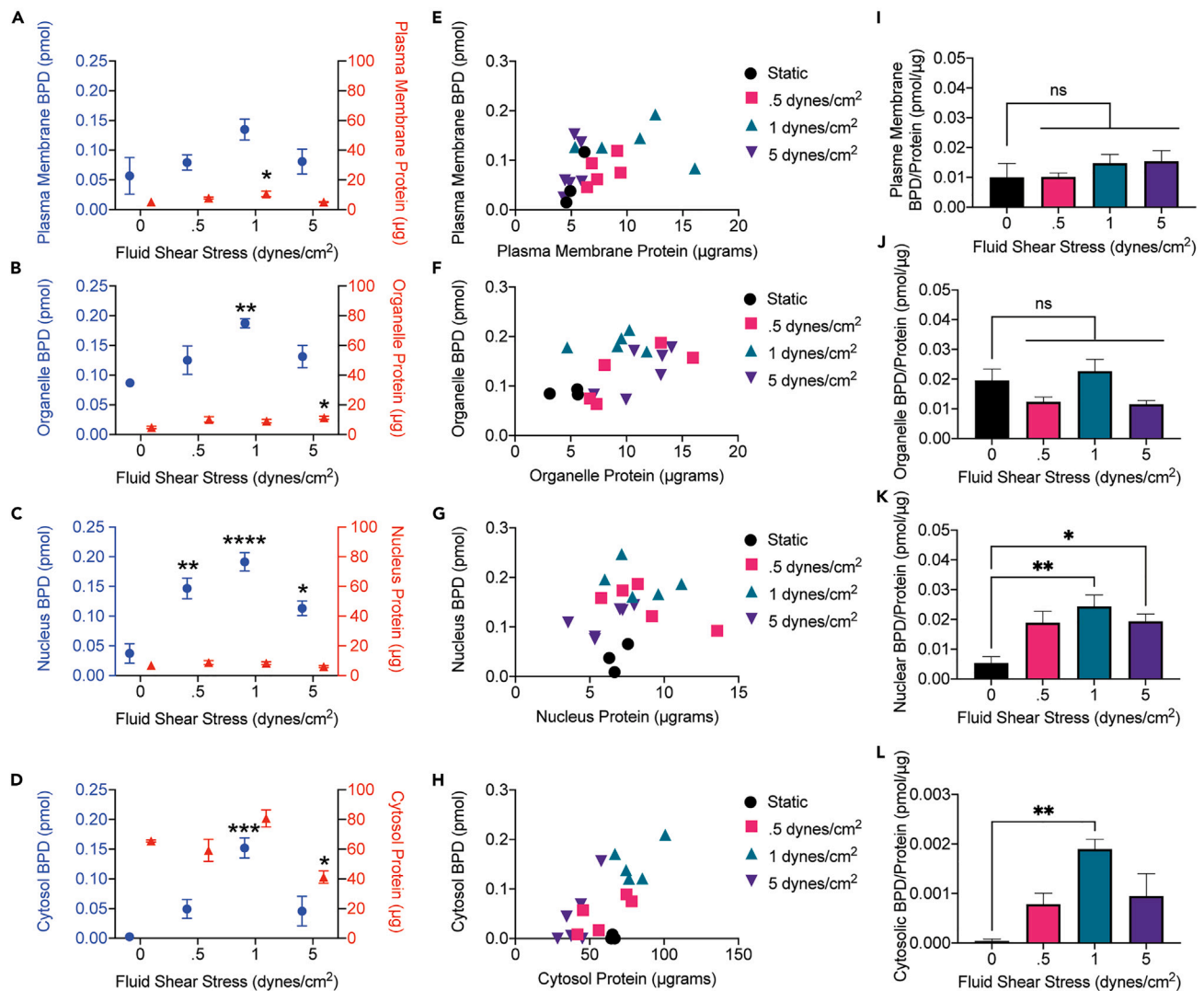
Figure 4. Fluid shear stress-dependent changes in subcellular BPD and protein compartmentalization

Monolayers of OVCAR8 cells were treated with 1 μM PIC under static or FSS (0.5, 1, 5 dyn/cm²) conditions and then fractionated for subcellular analysis of BPD, protein, and BPD/protein. FSS-dependent changes in BPD and protein (A–D). Individual datapoints for BPD versus protein (E–H). Normalized BPD/protein in each compartment (I–L). Statistical analysis was performed using a one-way ANOVA, and FSS data were compared to static controls using post hoc Dunnet test. Error bars represent the standard error of the mean. *p ≤ 0.05; **p ≤ 0.01; ***p ≤ 0.001; ****p ≤ 0.0001; ns: nonsignificant.

DISCUSSION

Cancers in the peritoneal cavity are currently treated with fluid flow-based drug delivery in the hyperthermic intraperitoneal chemotherapy (HIPEC) procedure, but the potential of transient flow as an amplifier of photochemical efficacy remains largely unknown. This paper sheds light on the potential application of transient flow in PIC delivery and the efficacy of EGFR-targeted PIT. Numerous models of flow-mediated drug delivery have been examined in previous work.[6,8,9,31–39] Recently, using a perfusion model with adherent 3D ovarian cancer nodules, we found that FSS (3 dyn/cm²) induced resistance to carboplatin, but not PIT.[9] The same study also showed that extended exposure to FSS (7 days) resulted in upregulation of phosphorylated ERK1/2 and EGFR. In contrast, Figure 1 shows a 13% decrease (p < 0.05) in EGFR expression following 30 min of exposure to FSS. There may, therefore, be kinetic variations in the biological effects of FSS on protein expression, internalization, and degradation. As recently reviewed by López-Hernández et al.,[40] cells may increase cellular endocytosis and subsequent lysosomal degradation of plasma membrane proteins in response to environmental stresses. In support of this, He et al. anchored hairpin-type fluorescent DNA probes to the cell surface to track the internalization of cell surface proteins under
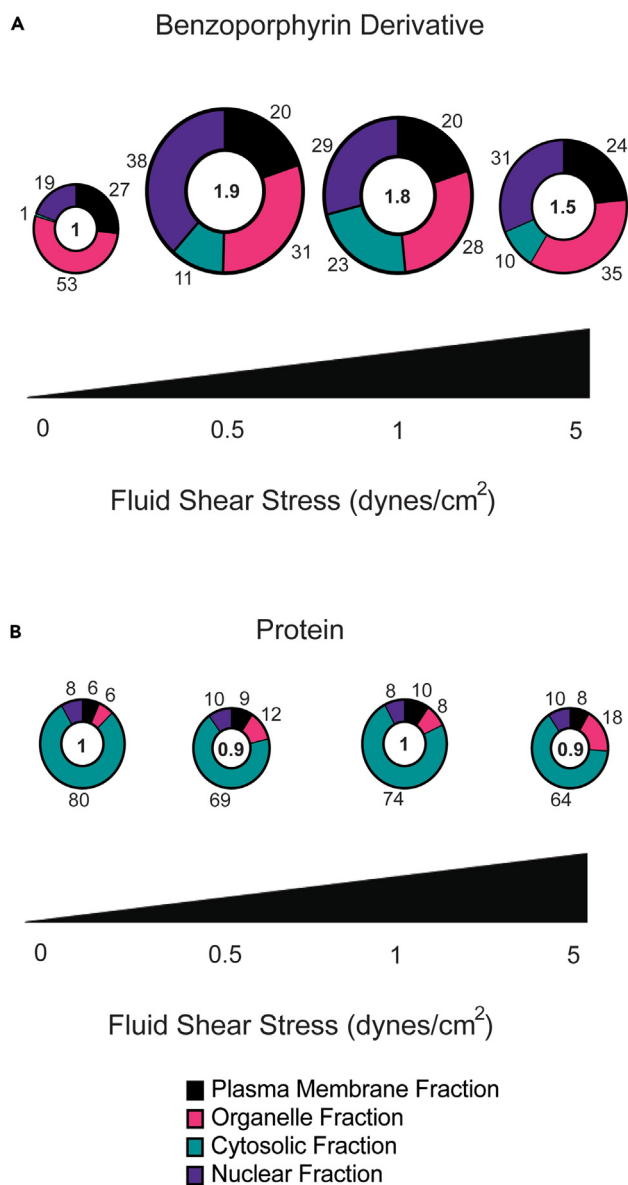
Figure 5. Percent distribution of BPD and protein among subcellular compartments

Total BPD (A) and total protein (B) values were summed across all compartments; then values in each compartment were divided by the sum to determine percentage. Circle diameter is equal to the fold change in total BPD or protein compared to static condition. Fold change is listed inside each circle. Compartment percentages are listed outside each segment.

FSS.[41] They found that FSS enhanced the endocytosis of plasma membrane proteins, resulting in probe localization at the mitochondria and lysosomes. Time-dependent effects of FSS on endothelial cell uptake of platelet endothelial cell adhesion molecule-1 (PECAM)-targeted nanoparticles were previously examined by Han et al.[8] They compared acute (30 min) versus chronic (16 h) FSS and uncovered opposing effects on uptake. Chronic FSS caused decreased nanoparticle uptake that was linked to morphological cellular alignment in the direction of flow and the formation of actin stress fibers. Treatment under acute FSS caused increases in nanoparticle uptake that were dependent on flow rate and number of antibodies per nanoparticle.

This is the first study, to our knowledge, to evaluate the dynamics of PIC binding and internalization in EGFR-expressing cancer cells under FSS. (Figures 2 and S1). Previous studies show that cetuximab-EGFR
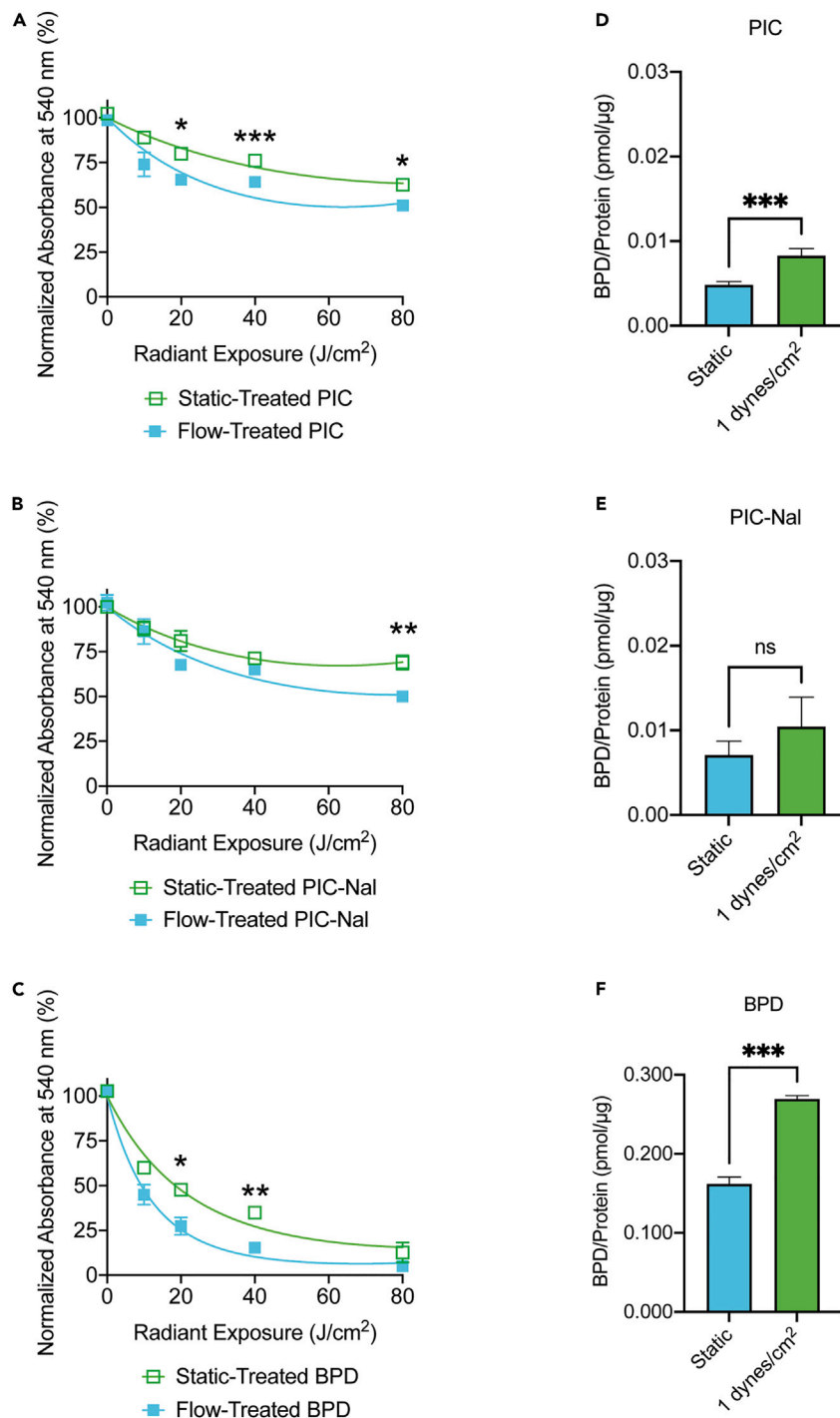
Figure 6. Cytotoxicity and uptake of three photosensitizer formulations following transient flow-mediated treatment

Confluent monolayers of OVCAR8 cells were treated with 1 μM PIC (A), 1 μM PIC-Nal (B), or 1 μM free BPD (C) for 30 min under static or FSS (1 dyn/cm^2) conditions. Next, medium was exchanged and chips were irradiated with a 690 nm laser at 10, 20, 40, or 80 J/cm^2 (100 mW/cm^2). After 4 h, cell viability was analyzed by NRU. For uptake studies, cells were incubated under static or FSS conditions with PIC (D), PIC-Nal (E), or BPD (F) and then immediately washed, collected, and analyzed as described in STAR Methods. Statistical analysis was performed using unpaired t tests. Error bars represent the standard error of the mean. *p ≤ 0.05; **p ≤ 0.01; ***p ≤ 0.001 ns: nonsignificant.

binding induces internalization of the cetuximab-EGFR complex, followed by trafficking to intracellular compartments including the endosome, lysosome, endoplasmic reticulum, and nucleus.[25–28] Work by Patel et al. found that when cetuximab binds to the EGFR-expressing cell surface, it begins internalization within minutes.[27] Localization increases gradually over the course of 4 h. Similarly, we showed that photosensitizer localization was detectable in the plasma membrane and organelles in as early as 10 min after incubation/ treatment, and accumulation plateaued after roughly 3 h (Figure 2). Our studies also revealed rapid nuclear localization, which was significantly enhanced under FSS culture after 30-min incubation. Consistent with these findings, Liao et al. showed, by western blot, that EGFR localizes to the nucleus as early as 30 min following incubation of MDA-MB-468 cells with cetuximab.

We next evaluated the effect of varying FSS (0.5, 1, 5 dyn/cm^2; 1.16, 2.31, 11.55 mL/min) on the total cellular (Figure 3) and subcellular (Figures 4 and 5) BPD, protein, and BPD/protein. The total cellular BPD and BPD/ protein increased significantly under 0.5 and 1 dyn/cm^2 compared to the static control (Figure 3). The total BPD and BPD/protein also increased at 5 dyn/cm^2; however, these changes did not reach statistical significance. Similar trends are seen within all subcellular compartments (Figure 4), where pmoles BPD increased at 0.5 and 1 dyn/cm^2 compared to the static condition and then began to decrease at 5 dyn/cm^2. This highlights a phenomenon previously shown in the literature in which an FSS "sweet spot" is achieved. Samuel et al. examined the effects of varying flow rate on the human umbilical vein endothelial cells (HUVEC) uptake of 2.7 nm quantum dots, 4.5 nm quantum dots, and 50 nm silica particles.[31] Uptake was most notably enhanced at moderate flow rates (0.05, 0.1 Pa), but the increase in uptake was less pronounced at the highest flow rate (0.5 Pa). Han et al. investigated the role of varying flow rate in the internalization of PECAM-targeted nanocarriers.[8] It was found that for particles with 50 antibodies per nanocarrier, uptake increased significantly between 1 and 4 dyn/cm^2 but not below 0.5 dyn/cm^2 or above 8 dyn/cm^2. Recently, Charwat et al. leveraged a complementary *in silico* and *in vitro* approach to evaluate the dynamic changes in uptake of 249 nm nanoparticles by endothelial cells under varying FSSs. They identified 1.8 dyn/cm^2 as the critical rate at which uptake is at a maximum. Above this rate, nanoparticle uptake decreased despite an increasing number of nanoparticles entering the system.

With increasing global use of HIPEC for intraperitoneal malignancies, FSS-based cancer treatment is a growing field of study. However, despite prior clinical use of photodynamic therapy for peritoneally disseminated cancers, the impact of FSS on photochemical treatments is largely unknown. In this study, three photosensitizer formulations were tested under FSS for the treatment of ovarian cancer *in vitro*. Multiple light doses were evaluated to account for light dose-dependent changes. All formulations exhibited trends toward greater cytotoxicity under FSS, with free BPD inducing the most cell killing compared to PIC and PIC-Nal (Figure 6). This is attributed to greatly enhanced uptake of free BPD compared to the antibody-based formulations. This is consistent with previous work that has shown enhanced uptake and anti-cancer effects of free photosensitizer compared to antibody-conjugated photosensitizer, though with the trade-off of poor cancer selectivity.[17–20,29] Additionally, unlike BPD and PIC, PIC-Nal uptake is not significantly enhanced under FSS-based treatment, though it trends toward an increase. Consistent with these observations, changes in toxicity under FSS are more modest for PIC-Nal compared to the other formulations. These formulation-based variations in uptake and cell killing are expected. As recently reviewed by Shurbaji et al., the effects of FSS on drug delivery and treatment effect are variable and depend on multiple factors including particle size, shape, charge, and elasticity.[2] Antibody-functionalized nanoparticles also vary in binding under FSS based on the number of antibodies per nanoparticle.[8] Based on these data, the clinical implementation of FSS-based photodynamic treatment will require careful consideration of nanoparticle properties and treatment parameters to enhance treatment outcomes.

In conclusion, this study examines the role of transient FSS as mediator of PIC delivery and interrogates the subsequent treatment effects with three photosensitizer formulations. We first confirm that the conjugation of the PIC remains stable and cell viability is not altered during treatment under transient FSS (Figure 1). Next, kinetic variations in photosensitizer delivery to subcellular compartments under static versus flow conditions are examined, revealing time-dependent changes in the BPD accumulation at the nucleus and cytosol (Figure 2). In contrast, BPD at the plasma membrane and organelles remains largely unchanged by treatment under FSS. FSS-dependent changes in total and subcellular BPD and protein are next evaluated, demonstrating the most significant increases in BPD accumulation at 0.5 and 1 dyn/cm^2 (Figures 3 and 4). We next evaluated subcellular compartmentalization of BPD and protein, revealing FSS-induced trends toward lower percent BPD at the organelles and higher percent BPD at the nucleus and

cytosol fractions (Figure 5). Total protein values do not change significantly in flow-treated cells; however, the compartmentalization of protein decreases at the cytosol by up to 16% and increases at the organelles by up to 12% between static and FSS conditions. Figure 6 shows the enhancement in phototoxicity of three photosensitizer formulations when treated under FSS compared to static conditions. Free photosensitizer, PIC, and PIC-coated liposomes all enhanced cell killing when administered at 1 dyne/cm^2. Overall, these preclinical data implicate flow-based treatment as a powerful parameter in the use of PIT for the treatment of peritoneally metastasized cancers.

Limitations of the study

It is critical to acknowledge several limitations of this study. One such consideration is that the clinical relevance of EGFR-targeted therapies for ovarian cancer remains ambiguous. Overexpression of the EGFR protein by ovarian cancers ranges widely from 9% to 62%.[42] Furthermore, efficacy of EGFR-targeted therapies for ovarian cancer has been limited.[43] As expertly reviewed by Bhandari et al.,[44] previous work shows that while the binding of EGFR-targeted PICs correlates with cellular EGFR expression, phototoxicity does not correlate with EGFR expression. This suggests that more factors are at play, such as the sensitivity of individual cancer cell lines. Still, EGFR-targeted PICs are at the forefront of clinical PIT, with one clinically used formulation in Japan and four clinical trials in the United States. Additionally, PIT is a platform technology, where various photosensitizers and antibodies can be conjugated to target specific tumor antigens that are relevant for different cancers. Therefore, information from this study could help to advance the development of PICs that target non-EGFR antigens for the treatment of ovarian cancer. Another limitation of this study is the variation between our flow model and physiological intraperitoneal flow. In this study, experiments are conducted under carefully controlled laminar flow, whereas flow in the peritoneal cavity is expected to be more turbulent. Further *in vivo* work is warranted to evaluate more physiologically relevant flow as a carrier for PICs.

STAR★METHODS

Detailed methods are provided in the online version of this paper and include the following:

- KEY RESOURCES TABLE
- RESOURCE AVAILABILITY
  - Lead contact
  - Materials availability
  - Data and code availability
- EXPERIMENTAL MODEL AND STUDY PARTICIPANT DETAILS
  - Cell culture
- METHOD DETAILS
  - Photosensitizer delivery under laminar flow
  - Total and subcellular photosensitizer delivery analysis
  - Cytotoxicity analysis
  - Synthesis and characterization of photoimmunoconjugates
  - Synthesis and characterization of Nanoliposomes (Nal) and photoimmunoconjugate-Nanoliposomes (PIC-Nal)
  - Lysate collection and western blotting
  - Confocal microscopy
- QUANTIFICATION AND STATISTICAL ANALYSIS

SUPPLEMENTAL INFORMATION

Supplemental information can be found online at https://doi.org/10.1016/j.isci.2023.107221.

scattering, and zeta potential experiments were conducted with support from the Bioworkshop at the University of Maryland, College Park, in the Fischell Department of Bioengineering.

AUTHOR CONTRIBUTIONS

A.J.S. and H.H. conceived and designed experiments; A.J.S., K.Z., C.L., I. Rahman, and K.McNaughton planned and performed *in vitro* study and analysis; A.J.S., K.May, and B.J.L. synthesized and characterized photoimmunoconjugates; A.J.S. and H.H. prepared the manuscript. B.J.L., C.L., D.M.R., and I.Rizvi suggested and commented on the design of experiments and translational aspects. All authors contributed to editing the final manuscript.

DECLARATION OF INTERESTS

The authors declare no competing interests.

INCLUSION AND DIVERSITY

We support inclusive, diverse, and equitable conduct of research.

REFERENCES

1. Szender, J.B., Emmons, T., Belliotti, S., Dickson, D., Khan, A.N.M.N., Morrell, K., Khan, A., Singel, K.L., Mayor, P.C., Moysich, K.B., et al. (2017). Impact of ascites volume on clinical outcomes in ovarian cancer: A cohort study. Gynecol. Oncol. *146*, 491–497. https://doi.org/10.1016/j.ygyno.2017.06.008.

2. Shurbaji, S., G Anlar, G., A Hussein, E., Elzatahry, A., and C Yalcin, H. (2020). Effect of Flow-Induced Shear Stress in Nanomaterial Uptake by Cells: Focus on Targeted Anti-Cancer Therapy. Cancers *12*, 1916.

3. Hyler, A.R., Baudoin, N.C., Brown, M.S., Stremler, M.A., Cimini, D., Davalos, R.V., and Schmelz, E.M. (2018). Fluid shear stress impacts ovarian cancer cell viability, subcellular organization, and promotes genomic instability. PLoS One *13*, e0194170. https://doi.org/10.1371/journal.pone.0194170.

4. Avraham-Chakim, L., Elad, D., Zaretsky, U., Kloog, Y., Jaffa, A., and Grisaru, D. (2013). Fluid-flow induced wall shear stress and epithelial ovarian cancer peritoneal spreading. PLoS One *8*, e60965. https://doi.org/10.1371/journal.pone.0060965.

5. Jeffrey, B., Udaykumar, H.S., and Schulze, K.S. (2003). Flow fields generated by peristaltic reflex in isolated guinea pig ileum: impact of contraction depth and shoulders. Am. J. Physiol. Gastrointest. Liver Physiol. *285*, G907–G918. https://doi.org/10.1152/ajpgi.00062.2003.

6. Rizvi, I., Gurkan, U.A., Tasoglu, S., Alagic, N., Celli, J.P., Mensah, L.B., Mai, Z., Demirci, U., and Hasan, T. (2013). Flow induces epithelial-mesenchymal transition, cellular heterogeneity and biomarker modulation in 3D ovarian cancer nodules. Proc. Natl. Acad. Sci. USA *110*, E1974–E1983. https://doi.org/10.1073/pnas.1216989110.

7. Ip, C.K.M., Li, S.-S., Tang, M.Y.H., Sy, S.K.H., Ren, Y., Shum, H.C., and Wong, A.S.T. (2016). Stemness and chemoresistance in epithelial ovarian carcinoma cells under shear stress. Sci. Rep. *6*, 26788. https://doi.org/10.1038/srep26788.

8. Han, J., Zern, B.J., Shuvaev, V.V., Davies, P.F., Muro, S., and Muzykantov, V. (2012). Acute and Chronic Shear Stress Differently Regulate Endothelial Internalization of Nanocarriers Targeted to Platelet-Endothelial Cell Adhesion Molecule-1. ACS Nano *6*, 8824–8836. https://doi.org/10.1021/nn302687n.

9. Nath, S., Pigula, M., Khan, A.P., Hanna, W., Ruhi, M.K., Dehkordy, F.M., Pushpavanam, K., Rege, K., Moore, K., Tsujita, Y., et al. (2020). Flow-induced Shear Stress Confers Resistance to Carboplatin in an Adherent Three-Dimensional Model for Ovarian Cancer: A Role for EGFR-Targeted Photoimmunotherapy Informed by Physical Stress. J. Clin. Med. *9*, 924–927. https://doi.org/10.3390/jcm9040924.

10. van Driel, W.J., Koole, S.N., Sikorska, K., Schagen van Leeuwen, J.H., Schreuder, H.W.R., Hermans, R.H.M., de Hingh, I.H.J.T., van der Velden, J., Arts, H.J., Massuger, L.F.A.G., et al. (2018). Hyperthermic Intraperitoneal Chemotherapy in Ovarian Cancer. N. Engl. J. Med. *378*, 230–240. https://doi.org/10.1056/NEJMoa1708618.

11. Sorrin, A.J., Kemal Ruhi, M., Ferlic, N.A., Karimnia, V., Polacheck, W.J., Celli, J.P., Huang, H.-C., and Rizvi, I. (2020). Photodynamic Therapy and the Biophysics of the Tumor Microenvironment. Photochem. Photobiol. *96*, 232–259. https://doi.org/10.1111/php.13209.

12. Spring, B.Q., Abu-Yousif, A.O., Palanisami, A., Rizvi, I., Zheng, X., Mai, Z., Anbil, S., Sears, R.B., Mensah, L.B., Goldschmidt, R., et al. (2014). Selective treatment and monitoring of disseminated cancer micrometastases in vivo using dual-function, activatable immunoconjugates. Proc. Natl. Acad. Sci. USA *111*, E933–E942. https://doi.org/10.1073/pnas.1319493111.

13. Mew, D., Wat, C.K., Towers, G.H., and Levy, J.G. (1983). Photoimmunotherapy: treatment of animal tumors with tumor-specific monoclonal antibody-hematoporphyrin conjugates. J. Immunol. *130*, 1473–1477.

14. Gui, T., and Shen, K. (2012). The epidermal growth factor receptor as a therapeutic target in epithelial ovarian cancer. Cancer Epidemiol. *36*, 490–496. https://doi.org/10.1016/j.canep.2012.06.005.

15. Nath, S., Saad, M.A., Pigula, M., Swain, J.W.R., and Hasan, T. (2019). Photoimmunotherapy of Ovarian Cancer: A Unique Niche in the Management of Advanced Disease. Cancers *11*, 1887. https://doi.org/10.3390/cancers11121887.

16. Ulfo, L., Costantini, P.E., Di Giosia, M., Danielli, A., and Calvaresi, M. (2022). EGFR-Targeted Photodynamic Therapy. Pharmaceutics *14*, 241.

17. Abu-Yousif, A.O., Moor, A.C.E., Zheng, X., Savellano, M.D., Yu, W., Selbo, P.K., and Hasan, T. (2012). Epidermal growth factor receptor-targeted photosensitizer selectively inhibits EGFR signaling and induces targeted phototoxicity in ovarian cancer cells. Cancer Lett. *321*, 120–127. https://doi.org/10.1016/j.canlet.2012.01.014.

18. Sorrin, A.J., Liu, C., Cicalo, J., Reader, J., Najafali, D., Zhang, Y., Roque, D.M., and Huang, H.-C. (2021). Photodynamic Priming Improves the Anti-Migratory Activity of Prostaglandin E Receptor 4 Antagonist in

Cancer Cells In Vitro. Cancers *13*, 5259. https://doi.org/10.3390/cancers13215259.

19. Liang, B.J., Pigula, M., Baglo, Y., Najafali, D., Hasan, T., and Huang, H.C. (2020). Breaking the selectivity-uptake trade-off of photoimmunoconjugates with nanoliposomal irinotecan for synergistic multi-tier cancer targeting. J. Nanobiotechnol. *18*, 1–14. https://doi.org/10.1186/s12951-019-0560-5.

20. Huang, H.-C., Pigula, M., Fang, Y., and Hasan, T. (2018). Immobilization of Photo-Immunoconjugates on Nanoparticles Leads to Enhanced Light-Activated Biological Effects. Small *14*, e1800236. https://doi.org/10.1002/smll.201800236.

21. Kessel, D., Luo, Y., Deng, Y., and Chang, C.K. (1997). The role of subcellular localization in initiation of apoptosis by photodynamic therapy. Photochem. Photobiol. *65*, 422–426. https://doi.org/10.1111/j.1751-1097.1997.tb08581.x.

22. Mahalingam, S.M., Ordaz, J.D., and Low, P.S. (2018). Targeting of a Photosensitizer to the Mitochondrion Enhances the Potency of Photodynamic Therapy. ACS Omega *3*, 6066–6074. https://doi.org/10.1021/acsomega.8b00692.

23. Oliveira, C.S., Turchiello, R., Kowaltowski, A.J., Indig, G.L., and Baptista, M.S. (2011). Major determinants of photoinduced cell death: Subcellular localization versus photosensitization efficiency. Free Radic. Biol. Med. *51*, 824–833. https://doi.org/10.1016/j.freeradbiomed.2011.05.023.

24. Mo, J., Mai Le, N.P., and Priefer, R. (2021). Evaluating the mechanisms of action and subcellular localization of ruthenium(II)-based photosensitizers. Eur. J. Med. Chem. *225*, 113770. https://doi.org/10.1016/j.ejmech.2021.113770.

25. Liao, H.-J., and Carpenter, G. (2009). Cetuximab/C225-induced intracellular trafficking of epidermal growth factor receptor. Cancer Res. *69*, 6179–6183. https://doi.org/10.1158/0008-5472.CAN-09-0049.

26. Okada, Y., Kimura, T., Nakagawa, T., Okamoto, K., Fukuya, A., Goji, T., Fujimoto, S., Sogabe, M., Miyamoto, H., Muguruma, N., et al. (2017). EGFR Downregulation after Anti-EGFR Therapy Predicts the Antitumor Effect in Colorectal Cancer. Mol. Cancer Res. *15*, 1445–1454. https://doi.org/10.1158/1541-7786.MCR-16-0383.

27. Patel, D., Lahiji, A., Patel, S., Franklin, M., Jimenez, X., Hicklin, D.J., and Kang, X. (2007). Monoclonal Antibody Cetuximab Binds to and Down-regulates Constitutively Activated Epidermal Growth Factor Receptor vIII on the Cell Surface. Anticancer Res. *27*, 3355–3366.

28. Jaramillo, M.L., Leon, Z., Grothe, S., Paul-Roc, B., Abulrob, A., and O'Connor McCourt, M. (2006). Effect of the anti-receptor ligand-blocking 225 monoclonal antibody on EGF receptor endocytosis and sorting. Exp. Cell Res. *312*, 2778–2790. https://doi.org/10.1016/j.yexcr.2006.05.008.

29. Savellano, M.D., and Hasan, T. (2005). Photochemical Targeting of Epidermal Growth Factor Receptor: A Mechanistic Study. Clin. Cancer Res. *11*, 1658–1668. https://doi.org/10.1158/1078-0432.Ccr-04-1902.

30. Björnmalm, M., Yan, Y., and Caruso, F. (2014). Engineering and evaluating drug delivery particles in microfluidic devices. J. Contr. Release *190*, 139–149. https://doi.org/10.1016/j.jconrel.2014.04.030.

31. Samuel, S.P., Jain, N., O'Dowd, F., Paul, T., Kashanin, D., Gerard, V.A., Gun'ko, Y.K., Prina-Mello, A., and Volkov, Y. (2012). Multifactorial determinants that govern nanoparticle uptake by human endothelial cells under flow. Int. J. Nanomed. *7*, 2943–2956. https://doi.org/10.2147/ijn.S30624.

32. Hosta-Rigau, L., and Städler, B. (2013). Shear Stress and Its Effect on the Interaction of Myoblast Cells with Nanosized Drug Delivery Vehicles. Mol. Pharm. *10*, 2707–2712. https://doi.org/10.1021/mp4001298.

33. Teo, B.M., van der Westen, R., Hosta-Rigau, L., and Städler, B. (2013). Cell response to PEGylated poly(dopamine) coated liposomes considering shear stress. Biochim. Biophys. Acta *1830*, 4838–4847. https://doi.org/10.1016/j.bbagen.2013.06.022.

34. Godoy-Gallardo, M., Ek, P.K., Jansman, M.M.T., Wohl, B.M., and Hosta-Rigau, L. (2015). Interaction between drug delivery vehicles and cells under the effect of shear stress. Biomicrofluidics *9*, 052605. https://doi.org/10.1063/1.4923324.

35. Kang, T., Park, C., Choi, J.-S., Cui, J.-H., and Lee, B.-J. (2016). Effects of shear stress on the cellular distribution of polystyrene nanoparticles in a biomimetic microfluidic system. J. Drug Deliv. Sci. Technol. *31*, 130–136. https://doi.org/10.1016/j.jddst.2015.12.001.

36. Kang, T., Park, C., and Lee, B.-J. (2016). Investigation of biomimetic shear stress on cellular uptake and mechanism of polystyrene nanoparticles in various cancer cell lines. Arch Pharm. Res. (Seoul) *39*, 1663–1670. https://doi.org/10.1007/s12272-016-0847-0.

37. Charwat, V., Olmos Calvo, I., Rothbauer, M., Kratz, S.R.A., Jungreuthmayer, C., Zanghellini, J., Grillari, J., and Ertl, P. (2018). Combinatorial in Vitro and in Silico Approach To Describe Shear-Force Dependent Uptake of Nanoparticles in Microfluidic Vascular Models. Anal. Chem. *90*, 3651–3655. https://doi.org/10.1021/acs.analchem.7b04788.

38. Nowak, M., Brown, T.D., Graham, A., Helgeson, M.E., and Mitragotri, S. (2020).

Size, shape, and flexibility influence nanoparticle transport across brain endothelium under flow. Bioeng. Transl. Med. *5*, e10153. https://doi.org/10.1002/btm2.10153.

39. Xu, Y., Qin, S., Niu, Y., Gong, T., Zhang, Z., and Fu, Y. (2020). Effect of fluid shear stress on the internalization of kidney-targeted delivery systems in renal tubular epithelial cells. Acta Pharm. Sin. B *10*, 680–692. https://doi.org/10.1016/j.apsb.2019.11.012.

40. López-Hernández, T., Haucke, V., and Maritzen, T. (2020). Endocytosis in the adaptation to cellular stress. Cell Stress *4*, 230–247. https://doi.org/10.15698/cst2020.10.232.

41. He, Z., Zhang, W., Mao, S., Li, N., Li, H., and Lin, J.-M. (2018). Shear Stress-Enhanced Internalization of Cell Membrane Proteins Indicated by a Hairpin-Type DNA Probe. Anal. Chem. *90*, 5540–5545. https://doi.org/10.1021/acs.analchem.8b00755.

42. Siwak, D.R., Carey, M., Hennessy, B.T., Nguyen, C.T., McGahren Murray, M.J., Nolden, L., and Mills, G.B. (2010). Targeting the epidermal growth factor receptor in epithelial ovarian cancer: current knowledge and future challenges. J. Oncol. *2010*, 568938. https://doi.org/10.1155/2010/568938.

43. Teplinsky, E., and Muggia, F. (2015). EGFR and HER2: is there a role in ovarian cancer? Transl. Cancer Res. *4*, 107–117. https://doi.org/10.3978/j.issn.2218-676X.2015.01.01.

44. Bhandari, C., Guirguis, M., Savan, N.A., Shrivastava, N., Oliveira, S., Hasan, T., and Obaid, G. (2021). What NIR photodynamic activation offers molecular targeted nanomedicines: Perspectives into the conundrum of tumor specificity and selectivity. Nano Today *36*, 101052. https://doi.org/10.1016/j.nantod.2020.101052.

45. Vázquez-Medina, J.P., Dodia, C., Weng, L., Mesaros, C., Blair, I.A., Feinstein, S.I., Chatterjee, S., and Fisher, A.B. (2016). The phospholipase A2 activity of peroxiredoxin 6 modulates NADPH oxidase 2 activation via lysophosphatidic acid receptor signaling in the pulmonary endothelium and alveolar macrophages. Faseb. J. *30*, 2885–2898. https://doi.org/10.1096/fj.201500146R.

46. Kutluay, S.B., Zang, T., Blanco-Melo, D., Powell, C., Jannain, D., Errando, M., and Bieniasz, P.D. (2014). Global Changes in the RNA Binding Specificity of HIV-1 Gag Regulate Virion Genesis. Cell *159*, 1096–1109. https://doi.org/10.1016/j.cell.2014.09.057.

47. Savellano, M.D., and Hasan, T. (2003). Targeting cells that overexpress the epidermal growth factor receptor with polyethylene glycolated BPD verteporfin photosensitizer immunoconjugates. Photochem. Photobiol. *77*, 431–439. https://doi.org/10.1562/0031-8655(2003)077<0431:tctote>2.0.co;2.

STAR★METHODS

KEY RESOURCES TABLE

REAGENT or RESOURCE	SOURCE	IDENTIFIER
Antibodies		
Rabbit monoclonal anti-EGFR	Cell Signaling Technology	Cat# 4267; RRID: AB_2246311
Rabbit monoclonal anti-GAPDH	Cell Signaling Technology	Cat# 2118; RRID: AB_561053
Chemicals, peptides, and recombinant proteins		
Verteporfin	Millipore Sigma	Cat# 1711461
Critical commercial assays		
Minute™ Plasma Membrane Protein Isolation and Cell Fractionation Kit	Invent Biotechnologies, Inc.	Cat# SM-005
Experimental models: Cell lines		
OVCAR8	Dr. Michael M. Gottesman	RRID: CVCL_1629
OVCAR3	Dr. Jocelyn Reader	RRID: CVCL_0465
J774	ATCC	RRID: CVCL_4692
Software and algorithms		
Graphpad Prism	GraphPad	N/A
Adobe Illustrator	Adobe	N/A
ImageJ	https://imagej.net/ij/index.html	N/A

RESOURCE AVAILABILITY

Lead contact

Further information and requests for resources and reagents should be directed to and will be fulfilled by the lead contact, Huang-Chiao Huang (hchuang@umd.edu).

Materials availability

This study did not generate new unique reagents.

Data and code availability

- All data reported in this paper will be shared by the lead contact upon request.
- This paper does not report original code.
- Any additional information required to reanalyze the data reported in this paper is available from the lead contact upon request.

EXPERIMENTAL MODEL AND STUDY PARTICIPANT DETAILS

Cell culture

OVCAR3 cells were obtained courtesy of Dr. Jocelyn Reader (University of Maryland School of Medicine), and OVCAR8 cells were obtained from Dr. Michael M. Gottesman (National Cancer Institute, National Institutes of Health). OVCAR8 and OVCAR3 cells were maintained in RPMI-1640 medium with L-glutamine (Corning) supplemented with 10% (OVCAR8) or 20% (OVCAR3) fetal bovine serum (Gibco), 100 U/mL penicillin and 100 μg/mL streptomycin (Lonza). J774 cells (ATCC) were maintained in DMEM (ATCC) supplemented with 10% fetal bovine serum, 100 U/mL penicillin and 100 μg/mL streptomycin. Cells were maintained at 37°C, 5% CO_2 incubator and subcultured at 80-90% confluence for less than 30 passages. Cells were confirmed free of mycoplasma using MycoAlert™ PLUS Mycoplasma Detection Kit (Lonza). Cell line biological identities were verified using STR profiling.

METHOD DETAILS

Photosensitizer delivery under laminar flow

The *in vitro* laminar flow model parameters are summarized in Table S1, and experimental workflow is shown in Figure S1. OVCAR8 cells were plated in the μ-Slide I$^{0.6}$ Luer chips at 250,000 cells/chip and incubated overnight. The following day, 1 μM photosensitizer was administered under flow using the Fluidic Unit Quad pump system and Pump Control Software (ibidi). The Fluidic Unit Quad pump system contains 4 perfusion sets, each accommodating one chip. Next, chips were either immediately collected for photosensitizer uptake analysis or light-activated for subsequent viability experiments. Static controls were collected by pipetting 200 μL treated medium directly into the chip. All treatments were conducted at 37°C, 5% CO$_2$, and dark controls were shielded from light throughout the treatment process. For each replicate in subcellular uptake studies, two chips were combined to accrue quantifiable amounts of BPD and protein within each fraction. Chips were not combined for total cellular uptake and cytotoxicity analyses.

Total and subcellular photosensitizer delivery analysis

Following photosensitizer treatment in static or flow conditions as described above, cells were lysed in radioimmunoprecipitation assay buffer (RIPA) (ThermoFisher) for total cellular analyses. For isolation of subcellular compartments (plasma membrane, organelle, cytosol, and nucleus) cell pellets were fractionated using the Minute™ Plasma Membrane Protein Isolation and Cell Fractionation Kit (Invent Biotechnologies, Inc.). Fluorescence (Ex/Em: 435 nm/700 nm; gain: 150) was measured using the synergy Neo2 (Biotek), and fluorescence values were compared to a standard curve to quantify BPD concentration in units of pmoles/L. Next, the Pierce™ BCA Protein Assay Kit (ThermoFisher Scientific) was used to quantify protein content in units of μgrams/L. Concentrations of BPD and protein were divided to determine pmoles BPD/μgrams protein. All fluorescence measurements were performed in black 96-well plates. The purity of the plasma membrane and organelle fractions has been previously characterized by Vázquez-Medina, et al. who showed that the plasma membrane fraction is enriched with plasma membrane markers such as Na$^+$/K$^+$-ATPase and flotillin, whereas the organelle fraction is enriched with markers for the mitochondria, Golgi, and endoplasmic reticulum.[45] Additionally, work by Kutluay et al. demonstrated that the cytosol fraction is enriched with cytosol marker LC3A/B.[46]

Cytotoxicity analysis

Following photosensitizer treatment, cells were irradiated using a 690-nanometer laser (10-80 J/cm^2, 100 mW/cm^2; Modulight, Inc.) and incubated for 4 hours prior to cytotoxicity analysis by Neutral Red Assay Kit (abcam). Briefly, after washing each chip with PBS, neutral red staining solution (prepared at 1x in cell culture media) was added to the chips and incubated for 2 hours at 37°C. The staining solution was then aspirated, and cells were washed and solubilized using buffers provided in the kit. The solubilized product was transferred to a 96 well plate, and absorbance at 540 nm was measured using the Synergy Neo2 (Biotek). Background-subtracted values were normalized to the untreated control to quantify lysosomal integrity.

Synthesis and characterization of photoimmunoconjugates

PICs were synthesized using carbodiimide chemistry as previously described.[19] 10kDa methoxy PEG succinimidyl carboxymethyl ester (mPEG-NHS; JenKem Technology) was reacted with cetuximab, BPD N-hydroxysuccinimidyl ester (BPD-NHS), and azide-PEG4-N-hydroxysuccinimidyl ester (azide-PEG-NHS) at a 3:1:6:2.5 molar ratio. Purification and buffer exchange were performed with 7 kDa MWCO Zeba™ spin desalting column (ThermoFisher) and 30 kDa MWCO Amicon® Ultra-15 Centrifugal Filter (Millipore Sigma), respectively. Final antibody and BPD concentrations were determined using Pierce™ BCA Protein Assay Kit (ThermoFisher Scientific) and UV-Vis spectroscopy. SDS-PAGE was used to measure purity. Final BPD:Cetuximab ratio was ~3:1, representing between 3- to 5-fold quenching.[12,47] To measure PIC stability under flow, PICs were flowed through cell-free chips for 30 minutes at 1 dynes/cm^2. The perfusate was collected for purity analysis via SDS-PAGE. Photoactivity was determined by dividing the maximum fluorescence intensity of PIC in PBS by the maximum fluorescence intensity of PIC in DMSO following excitation at 435 nm (Synergy Neo2, Biotek).

Synthesis and characterization of Nanoliposomes (Nal) and photoimmunoconjugate-Nanoliposomes (PIC-Nal)

For Nal synthesis, a mixture of dipalmitoylphosphatidylcholine (DPPC), dioleoylglycerophosphoglycerol (DOPG), cholesterol, distearoyl-phosphatidylethanolamine-methoxy polyethylene glycol (DSPE-mPEG2000), and distearoyl-glycerophosphoethanolamine-N-dibenzocyclooctyl polyethylene glycol (DSPE-mPEG2000-DBCO) was prepared at a 5.9:0.7:2.9:0.5:0.05 molar ratio in chloroform. All liposome components were purchased from Avanti. Chloroform was removed by rotary evaporation, then the dry lipid films were rehydrated in UltraPure™ DNase/RNase-Free Distilled Water (Invitrogen™). For liposome sizing, extrusion was performed through a 0.1 μm Nuclepore™ Track-Etched Polycarbonate Membrane Filter (Whatman). Copper-free click chemistry was used to generate PIC-Nal. PIC (containing azide) and Nal (containing DBCO) were mixed at a 90:1 molar ratio then purified using Sepharose CL-4B size exclusion chromatography. Size and zeta potential were quantified using the Nanobrook Omni (Brookhaven Instruments). PIC-Nal stability under flow and photoactivity were analyzed using the same methods as PIC.

Lysate collection and western blotting

Cellular proteins for western blotting were extracted as described previously.[18] Briefly, pelleted cells were lysed in radioimmunoprecipitation buffer (Thermo Fisher) supplemented with protease and phosphatase inhibitors (Thermo Fisher). Proteins were separated on NuPAGE™ 4 to 12% Bis-Tris gels (Invitrogen) then transferred to PVDF membranes (Thermo Scientific). Membranes were blocked in milk at room temperature for one hour, then probed overnight for epidermal growth factor receptor (EGFR) (1:1000, Cell Signaling #4267) and GAPDH (1:1000, Cell Signaling #2118). Primary antibody solutions were prepared in 5% bovine serum albumin (Fisher Scientific) dissolved in Pierce™ TBS Tween™ 20 Buffer (Thermo Fisher). Chemiluminescence was generated using SuperSignal™ West Pico PLUS Chemiluminescent Substrate (Thermo Fisher), then detected using the Azure 500 imager (Azure Biosystems). Image analysis was performed using imageJ. Background-subtracted EGFR band intensity was normalized first to GAPDH, then to the static control for quantification of relative protein expression.

Confocal microscopy

OVCAR8 cells were seeded in μ-Slide I$^{0.6}$ Luer chips (ibidi) at 250,000 cells/chip and incubated overnight for attachment. Next, 5 μM PIC treatment was administered under static or flow (1 dyne/cm^2) conditions for 5 hours. Cells were immediately fixed in 10% neutral buffered formalin (Millipore Sigma) for 15 minutes then stained with NucBlue™ Live ReadyProbes™ Reagent (Invitrogen). Confocal images were collected using a 405 nm laser with emission windows of 430-470 nm (nuclei) and 650-750 (BPD).

QUANTIFICATION AND STATISTICAL ANALYSIS

In this study, PRISM version 9.0.2 for MacOS was used for statistical analysis. ImageJ was used for quantification of photoimmunoconjugate purity and western blotting. Data were analyzed using unpaired t-test (where two groups are compared) and one-way ANOVA (where three or more groups are compared). Post-hoc tests used within each figure are specified in the figure captions. P values ≤ 0.05 were considered statistically significant, where * $p \leq 0.05$; ** $p \leq 0.01$; *** $p \leq 0.001$; **** $p \leq 0.0001$; ns: nonsignificant.